SUPPORTING INFORMATION

Table of Contents

Details of the Crystal Structure Refinement

Table S1. Crystal data and structure refinement for $Na_2[Rh_3Mn_3(CO)_{18}]$ (**2**).

Identification code	shelx
Empirical formula	C42 H48 Mn3 Na2 O24 Rh3
Formula weight	1456.33
Temperature	150.00(10) K
Wavelength	1.54178 Å
Crystal system	Orthorhombic
Space group	P n m a
Unit cell dimensions	a = 15.9667(8) Å α = 90°
	b = 18.5536(13) Å β = 90°
	c = 18.6281(17) Å γ = 90°
Volume	5518.4(7) $Å^3$
Z	4
Density (calculated)	1.753 Mg/m^3
Absorption coefficient	13.343 mm^{-1}
F(000)	2896
Crystal size	0.240 x 0.174 x 0.088 mm^3
Theta range for data collection	3.362 to 66.595°
Index ranges	-18<=h<=19, -22<=k<=18,
	-22<=l<=22
Reflections collected	20153
Independent reflections	5003 [R(int) = 0.0657]
Completeness to theta = 66.596°	99.4 %
Refinement method	Full-matrix least-squares on F^2
Data / restraints / parameters	5003 / 33 / 337
Goodness-of-fit on F^2	1.048
Final R indices [I>2sigma(I)]	R1 = 0.0780, wR2 = 0.2227
R indices (all data)	R1 = 0.1072, wR2 = 0.2495
Extinction coefficient	n/a
Largest diff. peak and hole	0.893 and -1.337
	$e.Å^{-3}$

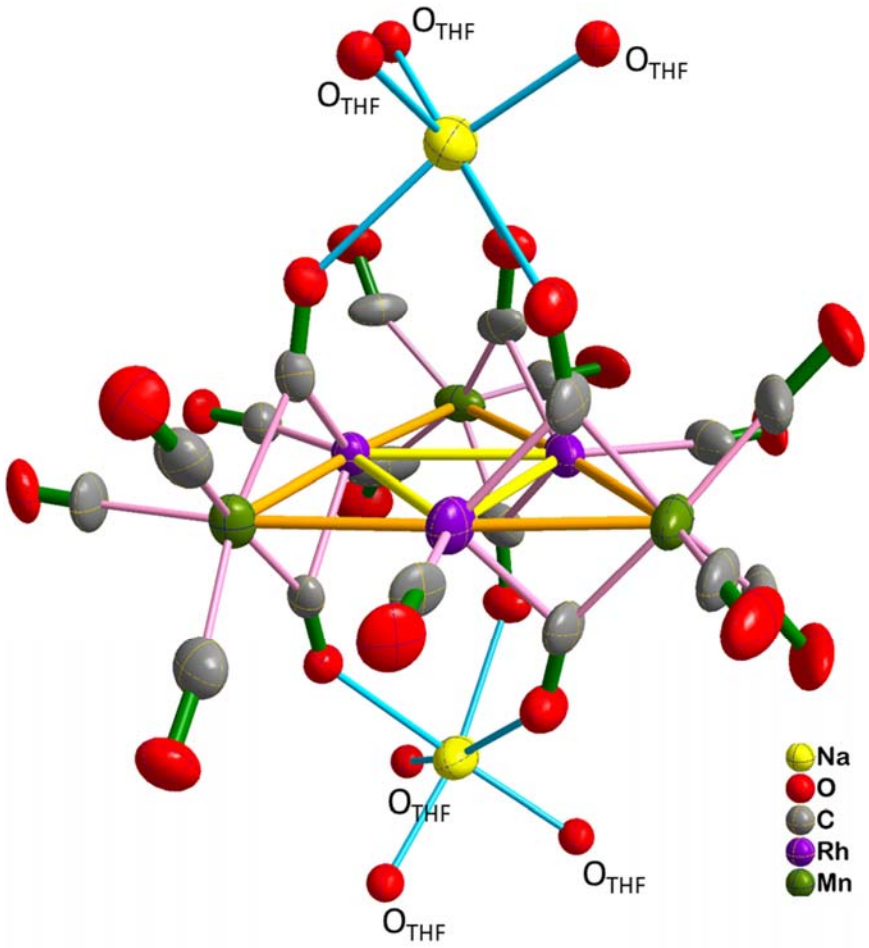

Figure S1. Molecular structure of the cluster of **2**. Thermal ellipsoids are drawn at 50 % probability level.

Details of the FTIR Measurements

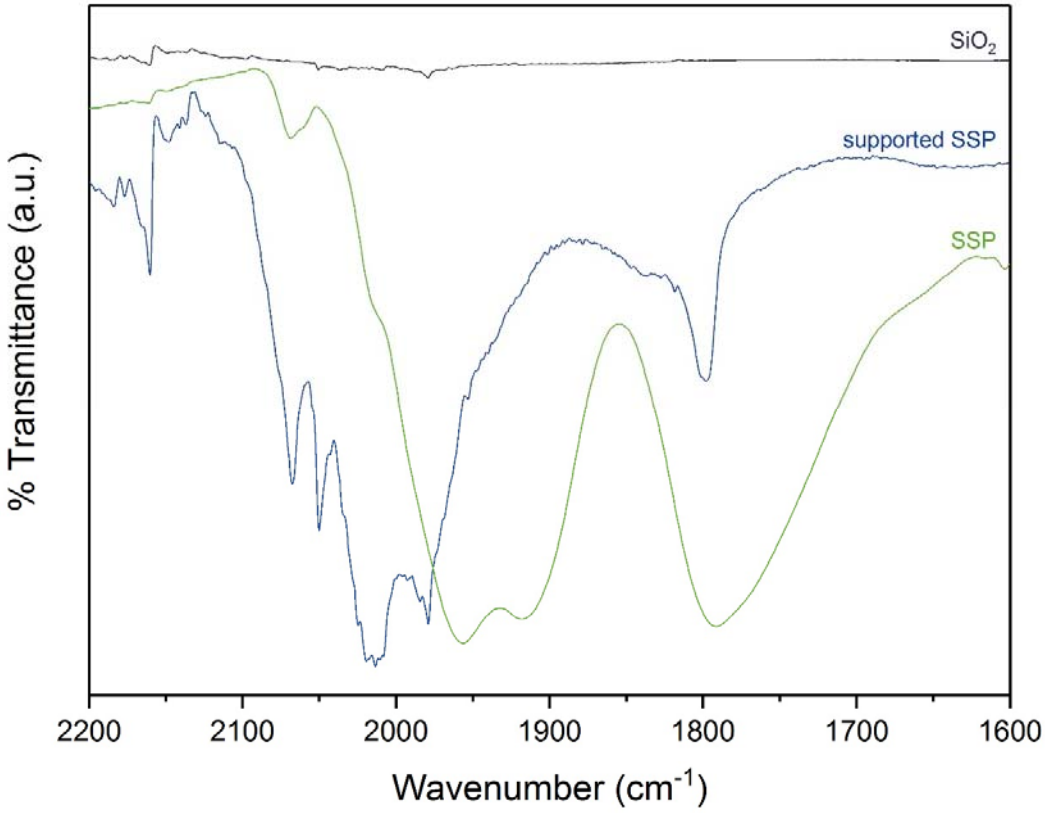

Figure S2. FTIR of silica-supported cluster $Na_2[Rh_3Mn_3(CO)_{18}]$ (**2**): The number of CO stretching vibration bands remains the same after impregnation and therefore also the overall symmetry of the cluster **2**. However, the bands of the terminal CO ligands are shifted to higher wavenumber which indicates less electron density at the hexanuclear metal core and a lower π backbonding. This can be explained by the chemisorption of the cluster **2** on the oxide support.

Details of the TPDe Studies

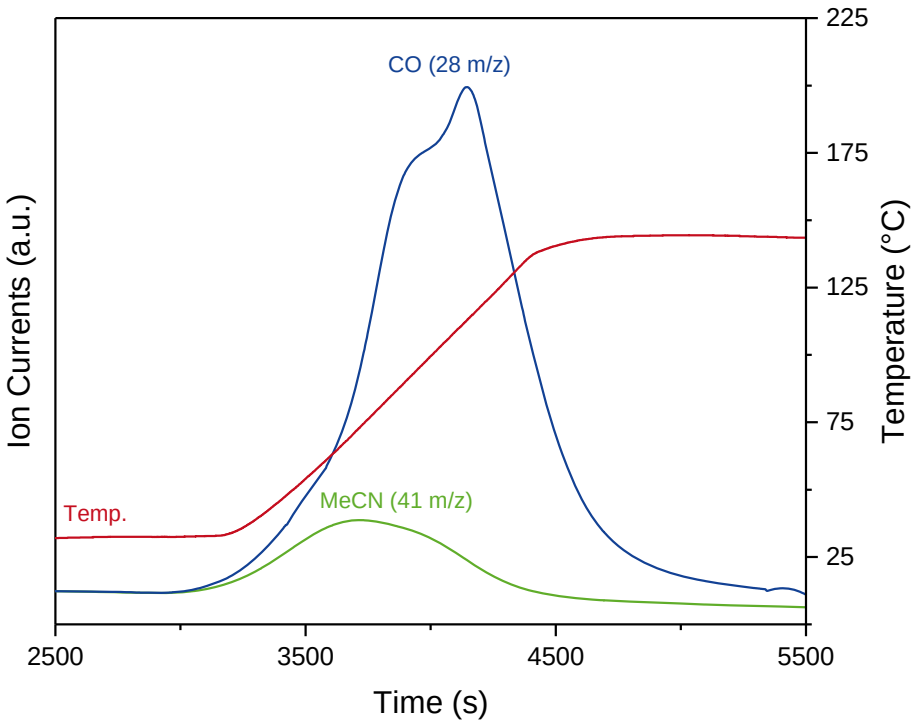

Figure S3. TPDe of silica-supported cluster $Na_2[Rh_3Mn_3(CO)_{18}]$ in 10 % H_2/He (2): The decomposition begins at approx. 70 °C (onset decarbonylation temperature) and reaches its first maximum at 96.4 °C which might be attributed to the weaker bonded bridging carbonyl ligands. Whereas the decarbonylation of the terminal CO ligands might lead to a second maximum at 113 °C. No other species were detected by MS with the exception of acetonitrile (41 m/z) which was used for the incipient wetness impregnation.

Details of the Catalysts Characterization

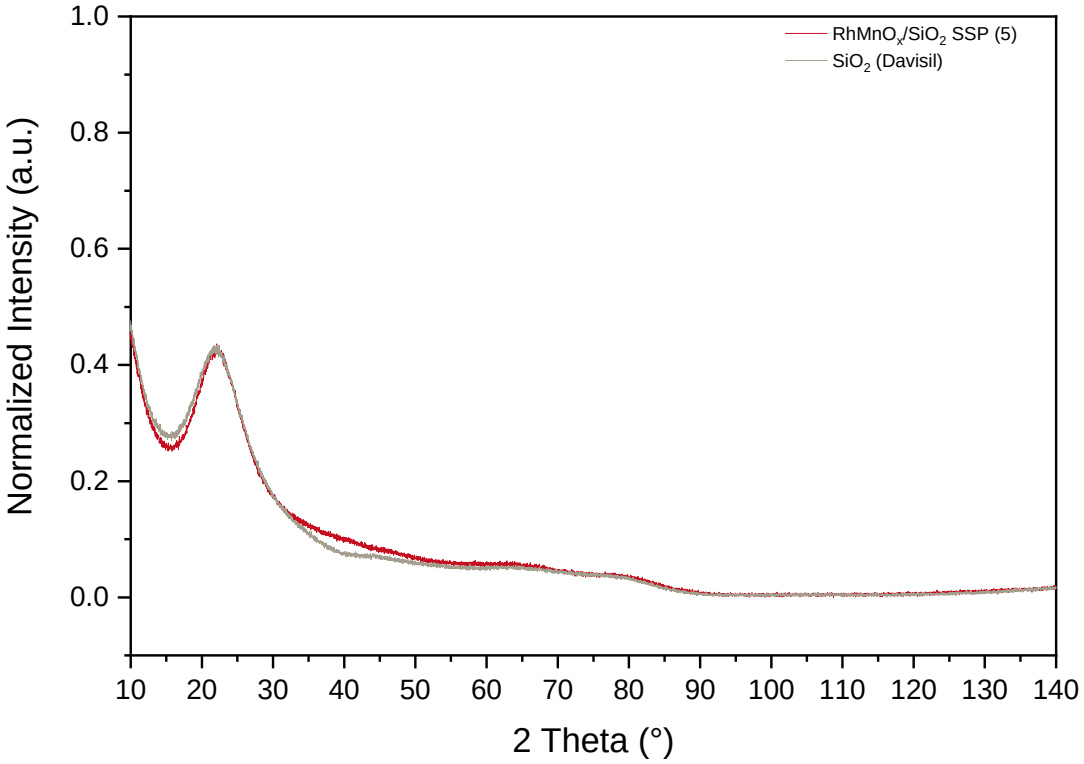

Figure S4. XRD raw data of the fresh $RhMnO_x/SiO_2$ SSP catalyst (5, red) in comparison with SiO_2 (Davisil, grey): A small deviation could be observed in the range of $2\theta = 41°$ which might be attributed to Rh(111) phase (40.77°). However, a phase identification cannot be conducted due to the XRD detection limit which is usually taken below a crystallite size of 3 nm. In addition to the (S)TEM images, the majority of the nanoparticles are relatively small and the investigated (S)TEM domains can be considered as representative for the characterized sample.

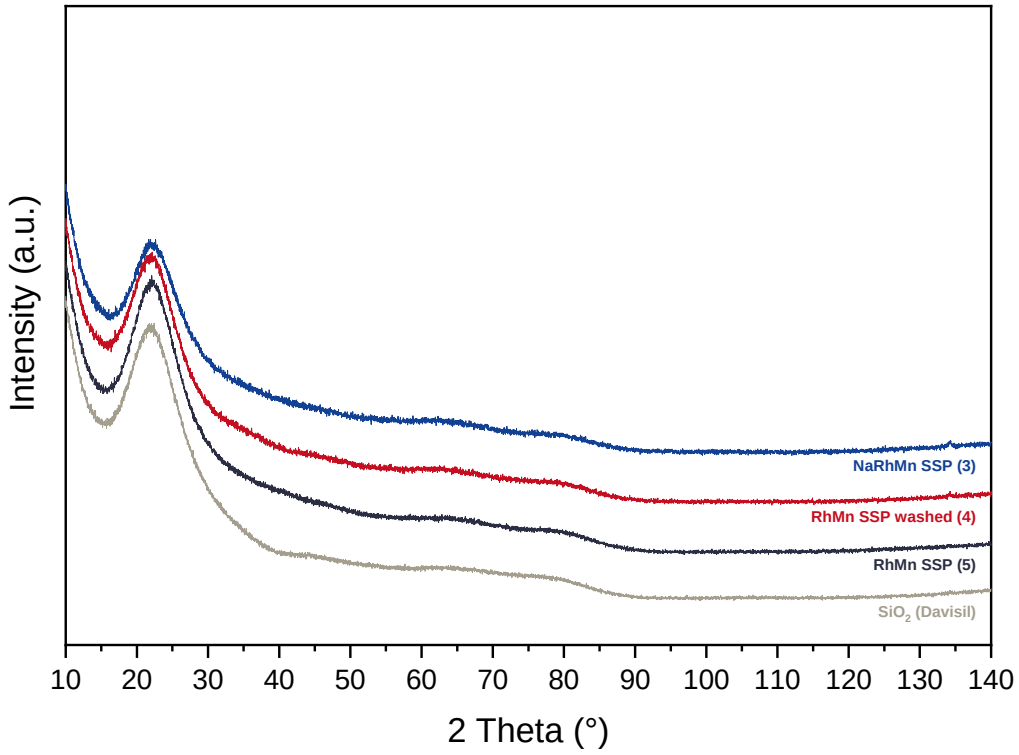

Figure S5. XRD raw data of fresh $NaRhMnO_x/SiO_2$ SSP (3, blue), $RhMnO_x/SiO_2$ SSP washed (4, red) and $RhMnO_x/SiO_2$ SSP (5, black) catalysts in comparison with SiO_2 (Davisil, grey).

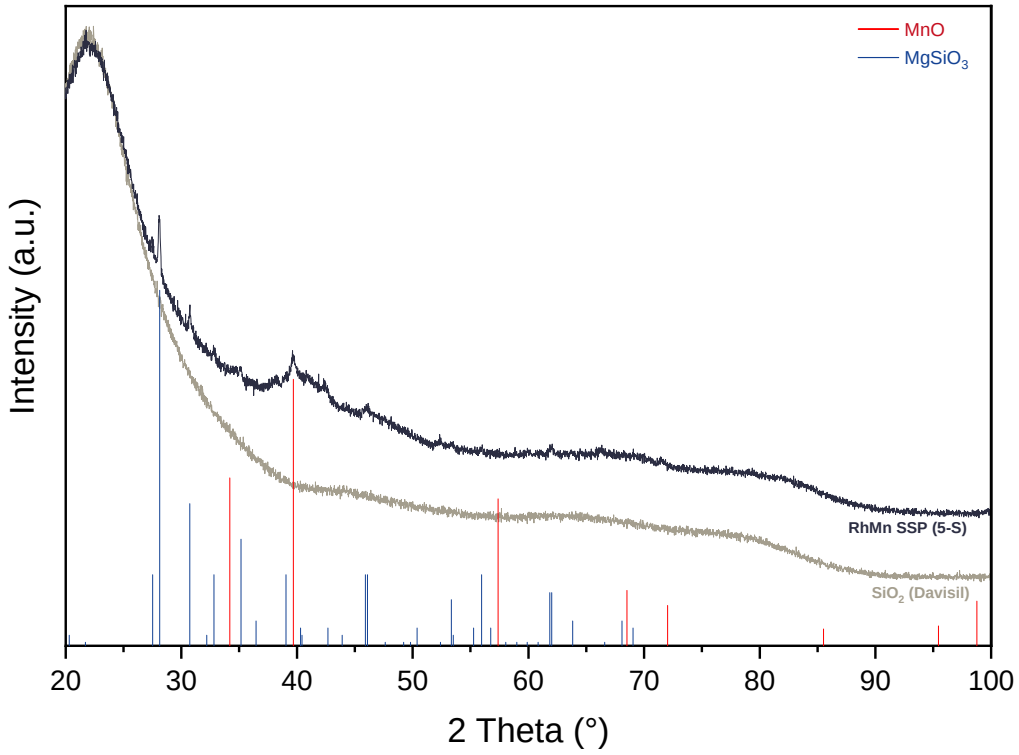

Figure S6. XRD raw data of the spent $RhMnO_x/SiO_2$ SSP catalysts (5-S, black) in comparison with SiO_2 (Davisil, grey): The detected diffractogram is in agreement with steatite (ICDD 011-0273) which was used as inert material in the catalytic test (see also the Experimental Section). The remaining reflection at $2\theta = 39.7°$ corresponds to the fcc{200} phase of MnO (ICDD 065-0638).

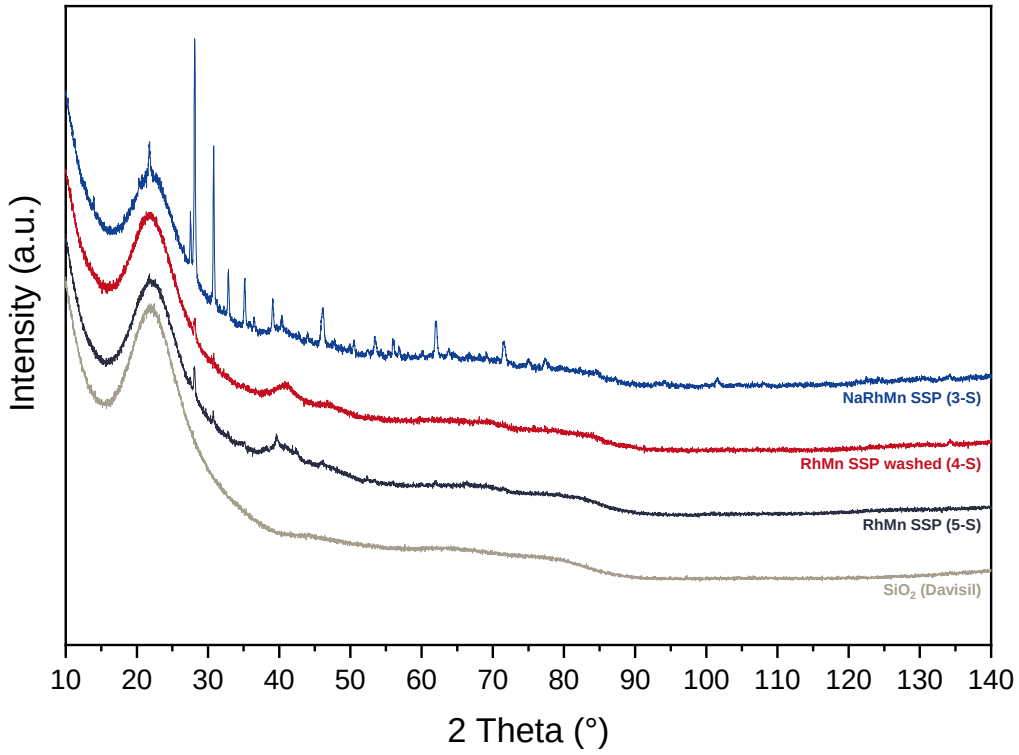

Figure S7. XRD raw data of spent $NaRhMnO_x/SiO_2$ SSP (3-S, blue), $RhMnO_x/SiO_2$ SSP washed (4-S, red) and $RhMnO_x/SiO_2$ SSP (5-S, black) catalysts in comparison with SiO_2 (Davisil, grey): Similar to the previously discussed diffractogram (Figure S6), the reflections are in agreement with steatite (ICDD 011-0273) which was used as inert material in the catalytic test. The difference in intensity is derived from the amount of steatite that could not be separated from the samples.

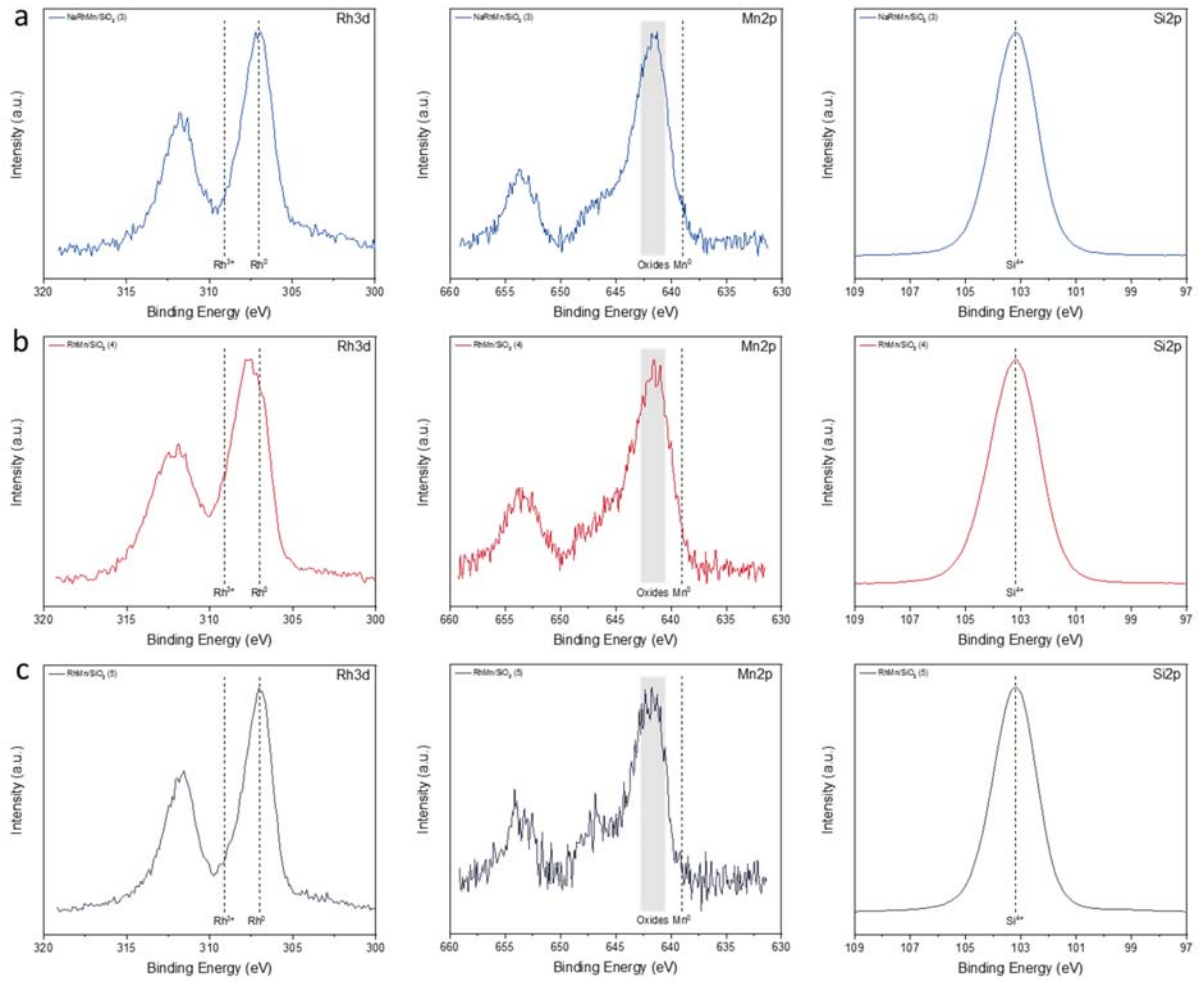

Figure S8. XPS data of the fresh (a) $NaRhMnO_x/SiO_2$ SSP (3), (b) $RhMnO_x/SiO_2$ SSP washed (4) and (c) $RhMnO_x/SiO_2$ SSP (5) catalysts: comparison of the Rh3d (left), Mn2p (middle) and Si2p (right) background-corrected spectra. Si2p (103.2 eV) was used as a binding energy reference.[1] All three samples show similar XPS results and the following explanation is consistent for the catalysts **3**-**5**. The electronic structure of rhodium is in agreement with the typical binding energy of metallic rhodium (307.0 eV).[2] An impact of Mn on the electronic structure of Rh is barely visible. Signals for metallic Mn (629.0 eV) in the Mn2p spectra (middle) cannot be found.[3] However, it is clearly visible that Mn is in an oxide state due to the common binding energy range of 641.1–643.4 eV.[4] These findings are in accordance to previously reported XPS data of

$RhMnO_x$ catalysts.[5] Si2p was used as a binding energy reference. The catalyst 4 was not handled under an inert gas atmosphere which leads to small shift in Rh^0 binding energy due to a partial oxidation.

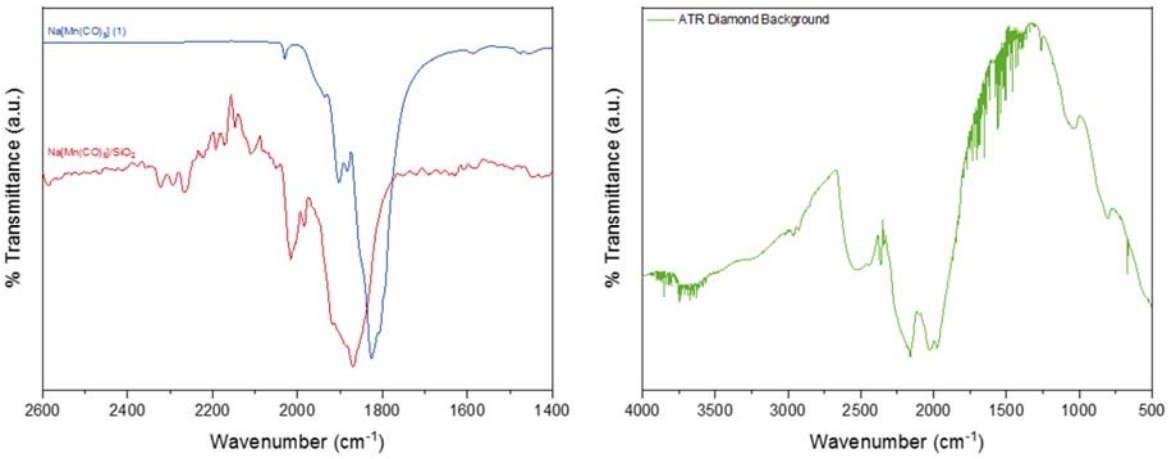

Figure S9. ATR-FTIR spectra of $Na[Mn(CO)_5]$ **1** before (red) and after incipient wetness impregnation in acetonitrile on silica (blue). The CO carbonyl stretching vibrations ν_{CO} are clearly shifted to higher wavenumbers implicating a stronger C-O bond accompanied by less electron density at the metal center and less π-back donation. This finding might be a indication for the oxidation of Mn(-I) to Mn(I) by formation of a $Mn^{I}(CO)_x(O_S)_{6-x}$ (x = 2–4) surface species which was also found for MgO-supported $Mn_2(CO)_{10}$.[6,7] The low signal to noise ratio in the supported metalate (red) is affect by the low nominal loading of approx. 6 wt%. The measurement artifact in the range of $\nu = 2050–2250\ cm^{-1}$ is attributed to the self-absorption of the used diamond ATR crystal and its low intensity in this range (see background spectrum on the left).

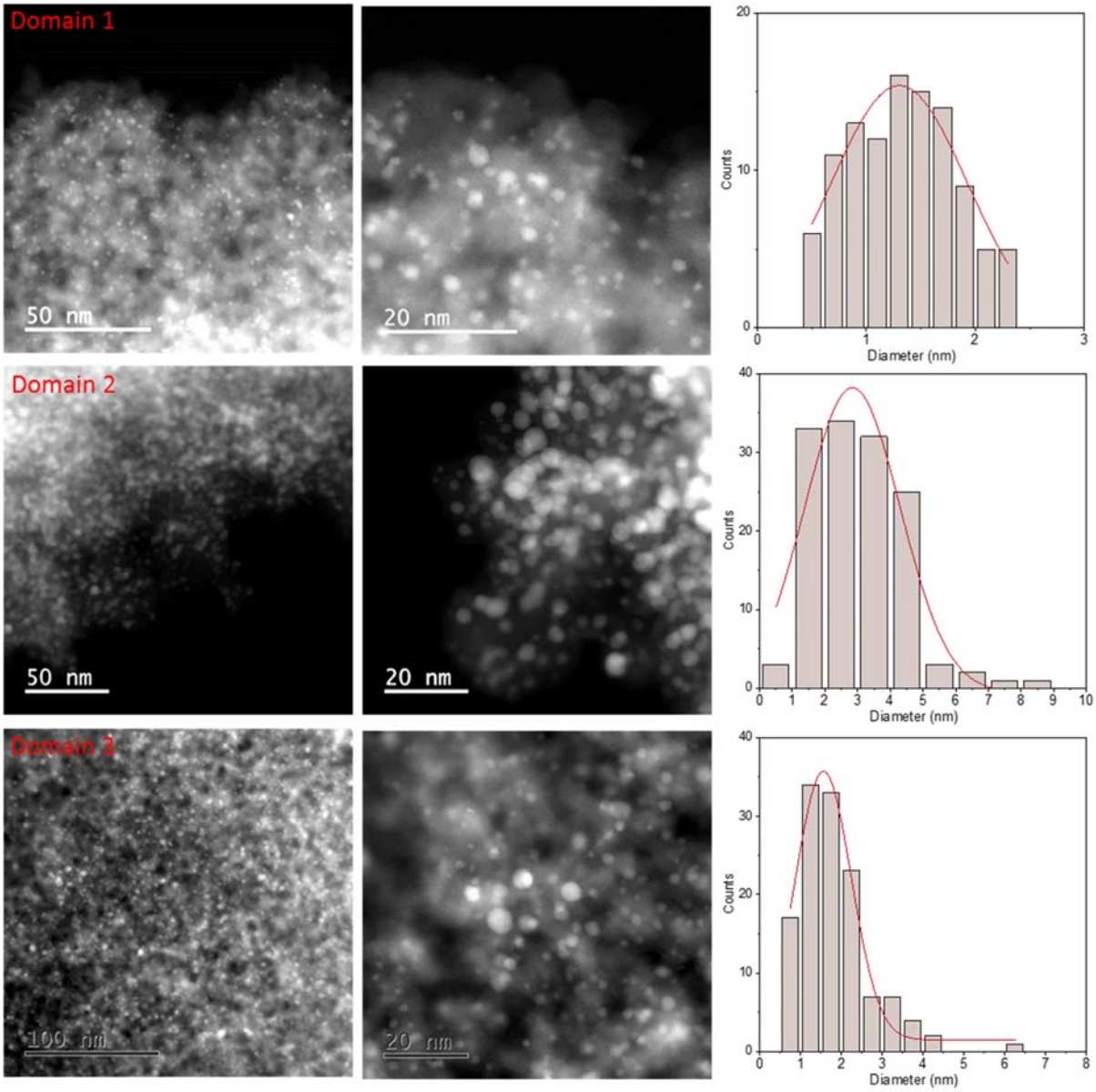

Figure S10. Additional ADF-STEM images of the fresh $RhMnO_x/SiO_2$ SSP catalysts (5): homogeneously dispersed nanoparticles with a mean particle size of 1.30, 2.80, and 1.55 nm and a narrow particle size distribution in domain 1, 2, and 3, respectively.

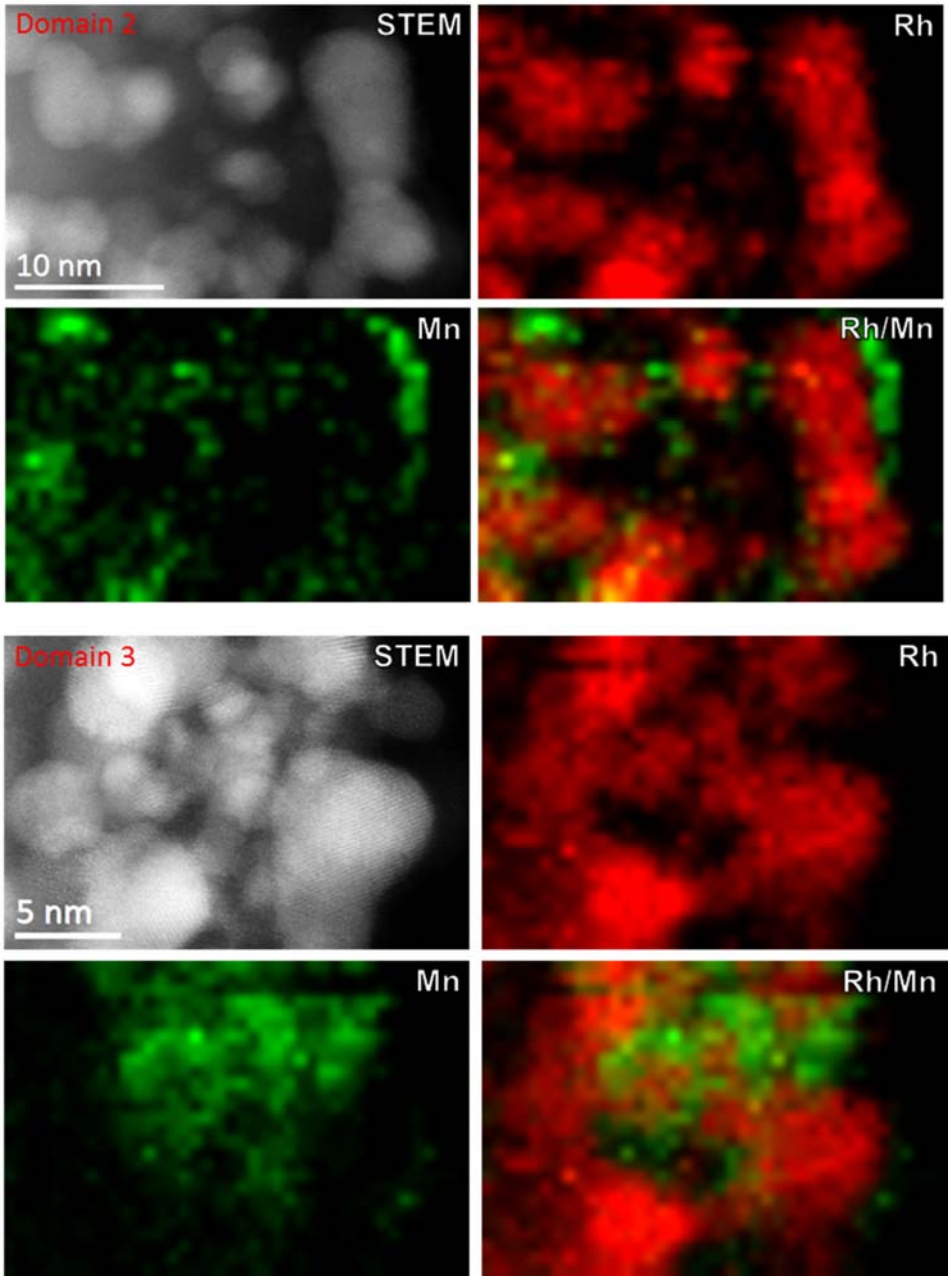

Figure S11. Additional composition analyses of the fresh $RhMnO_x/SiO_2$ SSP catalyst (5) by ADF-STEM with EDX mapping: Small particles of metallic rhodium (red) are closely contacted to a MnO_x species (green). No separated MnO_x or Rh nanoparticles could be found.

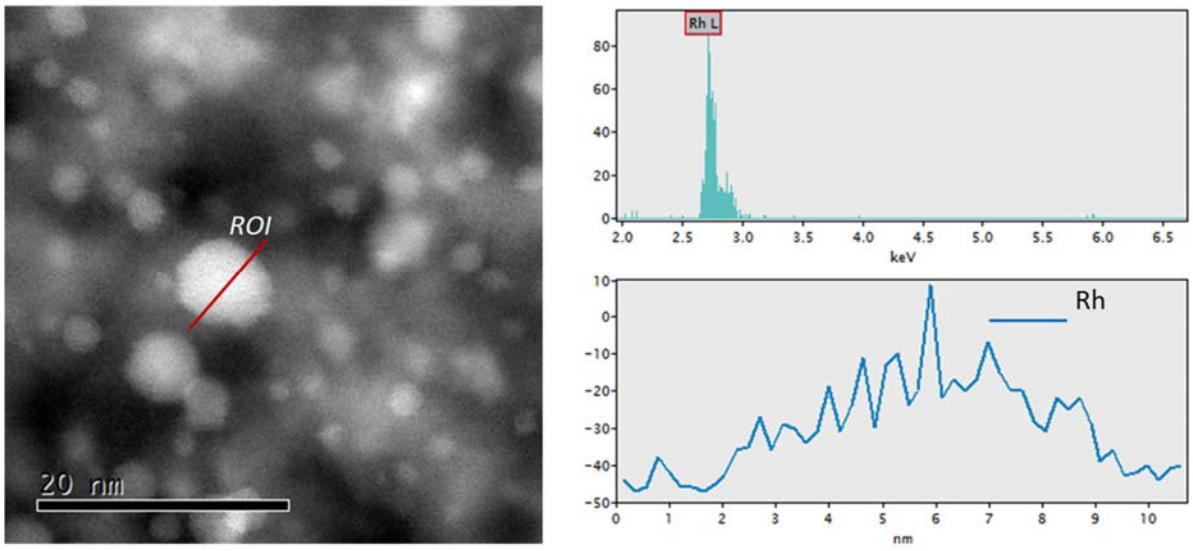

Figure S12. EDX line-scan profile of the fresh $RhMnO_x/SiO_2$ SSP catalyst (5).

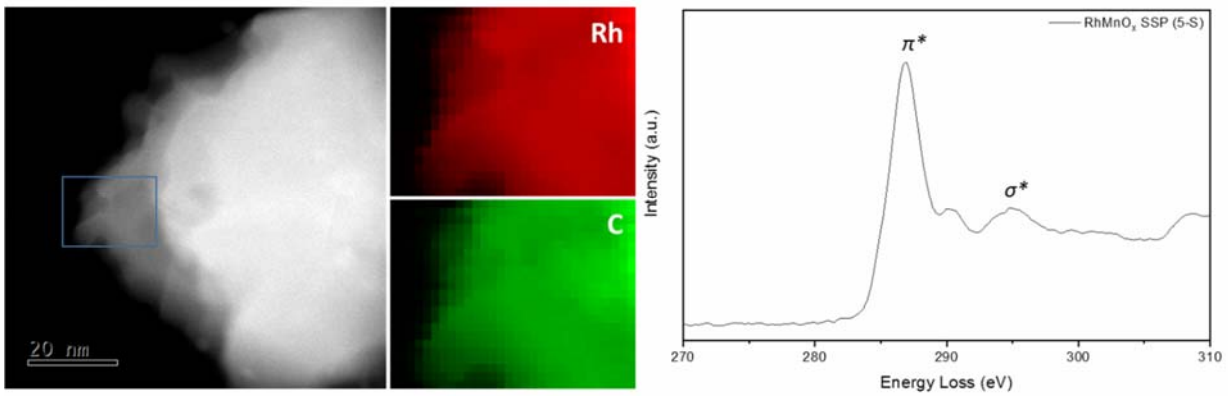

Figure S13. HAADF-STEM images of a sintered particle in the spent $RhMnO_x/SiO_2$ SSP catalyst (5-S) and the corresponding EELS spectrum with the carbon K edge fine structure of rhodium carbide: A sharp peak at 286.85 eV is observed corresponding to the excitations of 1s electrons to unoccupied π^* states. In addition, a broad band near 295 eV is attributed to the excitations to σ^* states.[8] The EELS spectrum resembles the spectra of metallic carbides and it is therefore assumed that a rhodium carbide RhC_x has been formed.[9] This assumption is in accordance to the clearly visible overlap of the Rh and C signals in the EELS maps.

Scheme of the Proposed Tilted Adsorption

Scheme S1. Proposed adsorption of CO at the $RhMnO_x$ interface in a tilted manner with a C atom bonded to Rh and the O atom bonded to MnO_x.[10]

Details of the Long-Term Stability Tests

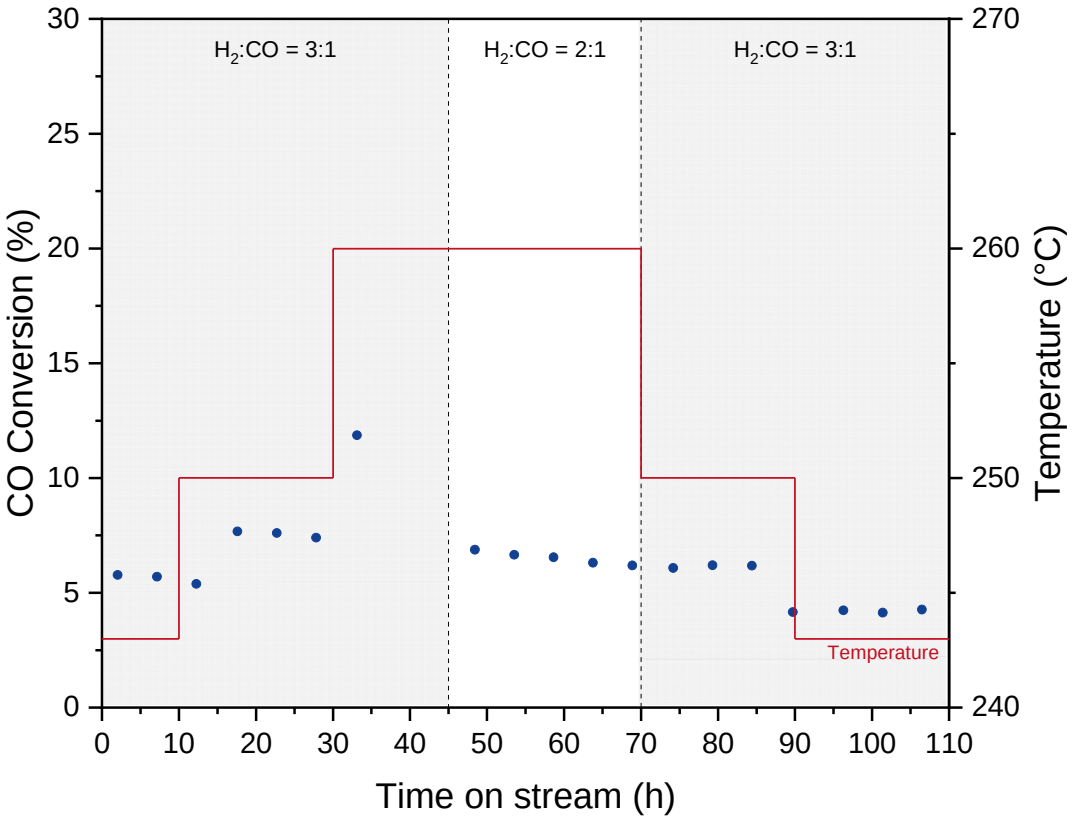

Figure S14. Long-term stability of the $NaRhMnO_x/SiO_2$ (3) SSP catalyst: Only a slightly deactivation can be observed after 105 h time-on-stream. Measuring conditions: 243–260 °C, 54 bar, GHSV 3500 h^{-1}.

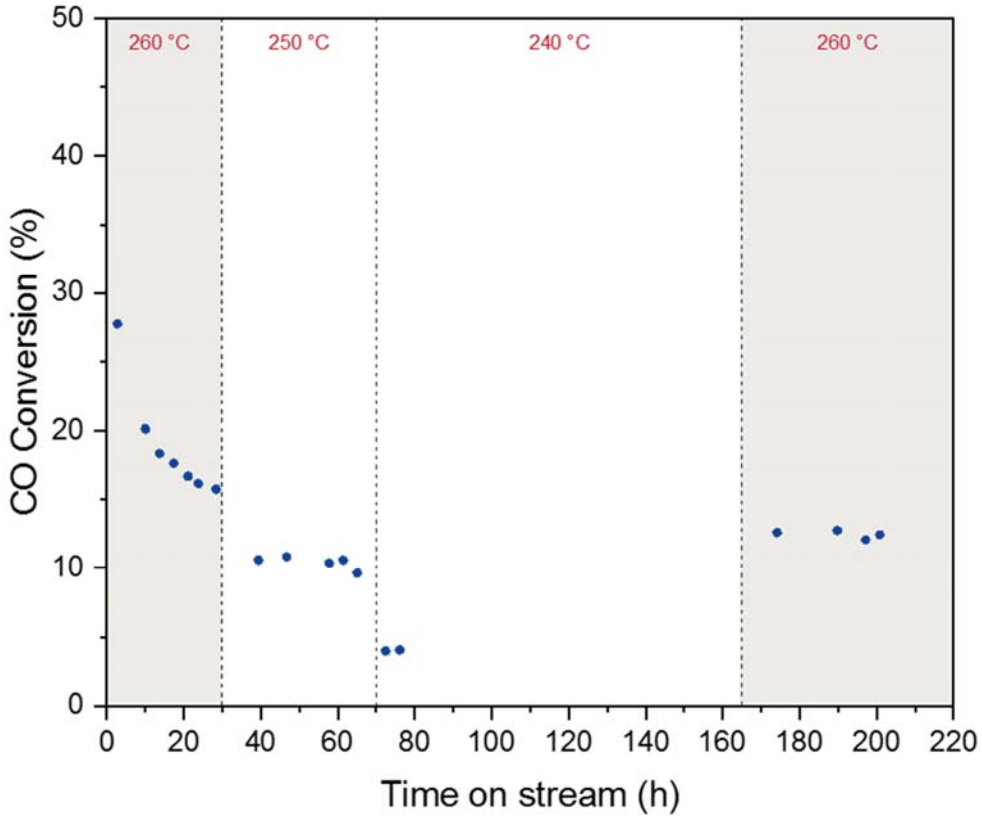

Figure S15. Long-term stability of the $RhMnO_x/SiO_2$ (5) SSP catalyst: In the first 20 h TOS, an initial decrease in CO conversion can be observed. After this initial phase, the catalyst is quite stable and shows only a slightly deactivation after additional 200 h TOS. Measuring conditions: 243–260 °C, 54.0 bar, $p(H_2)$ = 32.4 bar, p(CO) = 10.8 bar, GHSV 3500 h^{-1}.

Table of the Product Selectivities, Yields and Space Time Yields

Table S2. Catalytic activity and product selectivities of catalysts **3**–**6**, **8**, and a literature example.

Entry	Sample[a]	T (°C)	X_{CO} (%)	S_{CH_4} (%)	S_{MeOH} (%)	S_{EtOH} (%)	$S_{C_{2+}\,Oxy}$[b] (%)	$S_{C_{2+}\,HC}$ (%)	$S_{Olefins}$ (%)	Y_{EtOH} (%)	STY_{EtOH}[c] (µg/mg$_{Rh}$/s)
1	NaRhMnO$_x$/SiO$_2$ SSP (3)	260	11.9	37.1	8.70	19.5	45.9	5.32	2.93	2.32	0.60
2	RhMnO$_x$/SiO$_2$ SSP washed (4)	260	17.0	41.1	9.20	19.6	36.9	8.77	3.53	3.33	1.24
3	RhMnO$_x$/SiO$_2$ SSP (5)	260	17.5	37.7	0.20	24.1	52.0	7.96	3.56	4.22	1.06
4	RhMnO$_x$/SiO$_2$ Ref. (6)	250	17.9	44.8	4.78	15.7	40.5	9.96	3.61	2.81	0.58
5	RhMnO$_x$/SiO$_2$ Lit.[11]	270	17.0	39.2	0.8	17.7	46.0	13.2	-	3.01	-[d]
6	Rh/SiO$_2$ Ref. (8)	260	4.78	59.8	0.70	6.54	31.8	6.49	1.12	0.31	0.08
7	RhMnO$_x$/SiO$_2$ SSP (5)	260	27.7	39.5	0.66	23.6	52.0	6.43	1.01	6.54	1.64

[a]The catalysts were compared at iso-conversion (entry 1-5) after an initial deactivation phase. For catalysts **5**, the selectivity pattern is also provided at the highest measured conversion before deactivation (entry 7). Measuring conditions for tested catalysts **3**–**6**, and **8**: 250–260 °C, 54.0 bar, p(H$_2$) = 32.4 bar, p(CO) = 10.8 bar, GHSV = 3500 h^{-1}; for literature-known catalyst:[11] 270 °C, 30.0 bar, p(H$_2$) = 18 bar, p(CO) = 9 bar, GHSV = 4000 h^{-1}. [b]Mainly including ethanol, acetaldehyde and acetic acid. [c]Space time yield of ethanol calculated with the ethanol formation rate divided by active mass Rh (ICP-OES). [d]STYs per active mass Rh were not provided in the mentioned reference. They could not be calculated due to a lack of information (catalyst volume, flow rates, etc.) and may not comparable as a higher reaction temperature was used.

References

[1] M. R. Alexander, R. D. Short, F. R. Jones, M. Stollenwerk, J. Zabold, W. Michaeli, *J. Mater. Sci.* **1996**, *31*, 1879–1885.

[2] Y. OKAMOTO, N. ISHIDA, T. IMANAKA, S. TERANISHI, *Chem. Informationsd.* **1979**, *10*, DOI 10.1002/chin.197935137.

[3] A. R. Chourasia, D. R. Chopra, *Surf. Sci. Spectra* **1994**, *3*, 74–81.

[4] A. V. Naumkin, A. Kraut-Vass, S. W. Gaarenstroom, C. J. Powell, "NIST X-ray Photoelectron Spectroscopy Database, NIST Standard Reference Database Number 20" DOI 10.18434/T4T88K, **2012**.

[5] M. Dimitrakopoulou, X. Huang, J. Kröhnert, D. Teschner, S. Praetz, C. Schlesiger, W. Malzer, C. Janke, E. Schwab, F. Rosowski, H. Kaiser, S. Schunk, R. Schlogl, A. Trunschke, *Faraday Discuss.* **2018**, *208*, 207–225.

[6] M. P. Keyes, L. U. Gron, K. L. Watters, *Inorg. Chem.* **1989**, *28*, 1236–1242.

[7] S. Khabuanchalad, J. Wittayakun, R. J. Lobo-Lapidus, S. Stoll, R. D. Britt, B. C. Gates, *Langmuir* **2013**, *29*, 6279–6286.

[8] L. Alvarado Rupflin, J. Mormul, M. Lejkowski, S. Titlbach, R. Papp, R. Gläser, M. Dimitrakopoulou, X. Huang, A. Trunschke, M. G. Willinger, *ACS Catal.* **2017**, *7*, 3584–3590.

[9] Y. Jin, H. Xu, A. K. Datye, *Microsc. Microanal.* **2006**, *12*, 124–134.

[10] W. Mao, J. Su, Z. Zhang, X. C. Xu, D. Fu, W. Dai, J. Xu, X. Zhou, Y. F. Han, *Chem. Eng. Sci.* **2015**, *135*, 301–311.

[11] W. Mao, J. Su, Z. Zhang, X.-C. Xu, W. Dai, D. Fu, J. Xu, X. Zhou, Y.-F. Han, *Chem. Eng. Sci.* **2015**, *135*, 312–322.